Cr-doped La-Ni-O catalysts derived from perovskite precursors for CH_4-CO_2 reforming under microwave irradiation

Taiwo Odedairo[1], Jun Ma[2], Jiuling Chen[1]*, Zhonghua Zhu[1]*
[1]School of Chemical Engineering, The University of Queensland, St Lucia Brisbane Australia
[2]School of Engineering, University of South Australia, Mawson Lakes, SA, Australia
*Correspondence: Jiuling Chen (E-mail: cjlchen@yahoo.com), Zhonghua Zhu (E-mail: z.zhu@uq.edu.au), School of Chemical Engineering, The University of Queensland, St Lucia Brisbane Australia

Abstract

The nickel catalysts derived from Cr-doped $LaNiO_3$ perovskite-like precursors were characterized using XRD, HRTEM, TPO, TPR and XPS and their catalytic performance in CO_2 reforming of methane under microwave irradiation was investigated. It was found that the structure and morphology of the oxide composites in this research were influenced by the ratio of Ni and Cr and the mismatch of La^{3+}, Ni^{3+} and Cr^{3+} may cause the phase segregation. The catalytic performance of the Ni catalysts is dependent upon the oxygen mobility of perovskite oxide matrix, the content of the reduced Ni^0 and the content of the remaining perovskite structure. The mobile oxygen in the perovskite matrix in the catalyst may enhance the conversion of CO_2 during the reaction.
Keywords: Dry reforming, microwave irradiation, nickel, oxygen mobility, perovskite

1. Introduction

Carbon dioxide reforming of methane (dry reforming) has been attracting considerable attention for generating synthesis gas by transforming cheap two undesirable greenhouse gases, methane and carbon dioxide. The stoichiometric ratio of H_2/CO (1:1) in the produced synthesis gas in this process makes it to be an ideal feedstock for the further chemical process Fischer–Tropsch synthesis for producing high valuable liquid fuels [1–7].

Although the most active catalysts for dry reforming of methane (DRM) are noble metals (Rh, Ru, Pd and Pt) [8,9], their scarcity and high cost exclude them in industrial scale use. Nickel has been proved suitable to replace noble metals due to its comparative catalytic performance and low cost [10-13]. However, it is severely limited by suffering from the quick deactivation from the formation of the unreactive carbons deposited on the catalyst surface [14,15]. Up to now, different approaches are practised on suppressing, reducing and even removing the deposited carbons from catalyst surface. Promising strategies to address these challenges include (i) doping a small amount of promoters into Ni catalysts [6,16-18], (ii) generating nano-sized Ni particles by strengthening the interaction between Ni particles and the carrier [1,2,7], and (iii) improving the particles dispersion on the carrier [6,7,19].

Received: November 23, 2015; revised: January 22, 2016; accepted: April 22, 2016

To be cited as: Chem. Eng. Technol. 10.1002/ceat.201500702

Link to final VoR: http://dx.doi.org/10.1002/ceat.201500702

Among them an attractive option is to take advantage of the ABO_3 perovskite-like structure oxides as the catalyst precursor for obtaining the highly dispersed Ni particles embedded in the oxide matrix under the reaction conditions as a result of the precursor reduction [19-22]. In an ABO_3 structure where 'A' and 'B' are two cations of very different sizes and O is an anion that bonds to both, the 'A' atoms are larger than the 'B' atoms and A ion can be rare-earth or alkaline-earth metal, such as La, Ca, Sr, Ce and Pr that fits in to the dodecahedral site of the framework and the B ion is transition metal ions such as Fe, Co, Cr and Ni which occupy the octahedral sites [20-22]. Therefore, the advantage for employing a perovskite structure as the catalyst precursor is that the structural and thermal stability as well as the catalytic activity can be adjusted by the substitution with various cations on A and/or B sites. The high dispersion of Ni particles prepared from a $LaNiO_3$ perovskite precursor has been obtained to demonstrate a high activity and stability owing to the participation of mobile oxygen of the oxide matrix in the reaction thus preventing the catalyst coking during DRM [20,21].

Microwave energy is cost-effective in comparison with the conventional heating systems [3,23-25]. It can heat some certain catalysts directly and uniformly throughout their volume instead of through its outer surface in conventional heating system. It has been increasingly used for the growth of carbon materials [15,25,26], but only a few studies have adopted it for syngas production [3,4]. The results in publication and in our lab have illustrated that the combination of microwave heating and Ni catalysts can give rise to conversions of both CO_2 and CH_4 in DRM [4,27]. $LaNiO_3$ is a strong microwave receptor, and can be effectively heated under microwave irradiation [28,29]. In this investigation, to further improve the stability of high-dispersed Ni particles, Cr-doped $LaNiO_3$ perovskite-like structure was employed as the catalyst precursor in which Ni will be substituted with Cr^{3+} in Ni^{3+} sites partially (B sites in ABO_3) and the influence of the doping amount of Cr on the performance of the catalyst under microwave irradiation was investigated. The reason of selecting Cr as the dopant/promoter is because i) $LaCrO_3$ shows great stability for applications involving high temperature [30], ii) The size of Cr^{3+} (0.615 Å) is similar as that of Ni^{3+} (0.60 Å) and hence the doping of Cr may not cause a big distortion of the perovskite structure [31], and iii) $LaCrO_3$ is a good microwave energy absorber and the incorporation of Cr will not affect the absorption of microwave energy of the catalyst system [32].

2. Experimental

2.1. Materials

Metal precursors, including nickel nitrate ($Ni(NO_3)_2{\cdot}6H_2O$), lanthanum nitrate ($La(NO_3)_3{\cdot}6H_2O$), chromium nitrate ($Cr(NO_3)_3{\cdot}9H_2O$), urea (NH_2CONH_2) and sodium hydroxide (NaOH) were all purchased from Sigma Aldrich and used as received.

2.2. Synthesis of mixed oxide composites with different structures

We in this study developed a urea-based co-precipitation method to synthesize a number of $LaCr_{1-x}Ni_xO_{3-\delta}$ where x = 0.1, 0.4 and 0.7, and the relevant products were respectively denoted as LCN-1, LCN-4 and LCN-7 (Table 1). In details, stoichiometric amounts of $La(NO_3)_3{\cdot}6H_2O$ and $Cr(NO_3)_3{\cdot}9H_2O$ were dissolved in deionized water and stirred continuously at 60 °C for 5 h. This was followed by addition of 50 mL of urea solution (0.75 mol/L) under continuous stirring at 60 °C, and then kept stirring for 3 h. A calculated amount of $Ni(NO_3)_2{\cdot}6H_2O$ was then added into the solution at 60 °C and stirred for 5 h *and the solution was close neutral (pH≈7.5)*. While the Ni fraction may change, the molar ratio of the total metal ions to urea was set at 1:3. 10 mL of NaOH solution (0.5 mol/L) was added to the above solution in drops at 120 °C, and stirred continuously for 2 h *and the pH of the suspension was kept around 12*. The precipitates were filtered, washed with deionized water and absolute ethanol 3 times, and left to dry overnight at 120 °C. The sample was then calcined in air at 850 °C for 5 h.

2.3. Characterization of structures

The structure phase of LCNs was determined by X-ray diffraction (XRD) in a Bruker Advanced X-ray diffractometer using nickel-filtered Cu Kα X-ray source radiation. Le Bail and Rietveld refinements on the XRD patterns were conducted using DIFFRAC^{plus} Topas 4.2 software. The high resolution transmission electron microscopy (HRTEM) was recorded on a JEOL 2100 microscope operated at 200 kV. X-ray photoelectron (XPS) spectra were acquired on a Kratos Axis ULTRA X-ray photoelectron spectrometer.

Temperature-programmed desorption (TPD) of O_2 on the catalysts was studied on a BELCAT (BEL Japan, INC) and the oxygen signal was monitored by a BELMASS mass spectrometer in Ar flow while heating from 50 to 850 °C at a rate of 10 °C/min. The reducibility of catalysts was studied by hydrogen temperature programmed reduction (H_2-TPR) employing the above BELCAT and the specie signal s of hydrogen and water were monitored by the above mass spectrometer. In each TPR, the samples (50 mg) were placed at the bottom of a U-shaped quartz and was heated in 5 vol.%H_2/Ar of 50 ml/min at a heating rate of 10 °C/min from 50 to 850 °C. The hydrogen consumption was monitored by mass spectrometer. Before the H_2-TPR analysis, the samples were heated for 60 min in Ar flow at 100 °C.

The *in situ* CH_4-CO_2 temperature-programmed reaction was investigated on BELCAT. It was performed on 20 mg of LCN-1 or LCN-4 in 10%CH_4/10%CO_2 in N_2 (50 ml/min) at a heating rate of 5 °C/min from 50 to 850 °C. The above mass spectrometer was employed to monitor the masses of interest. The different mass fragments were recorded as a function of temperature to monitor the reaction products i.e. methane (*m/e* 16 and 15), CO_2 (*m/e* 44), water (*m/e* 18 and 17), H_2 (*m/e* 2) and CO (*m/e* 28). CO has a major peak at *m/e* 28 which unfortunately overlaps with N_2, and so CO and N_2 cannot be distinguished herein.

2.4. Effect of structure on catalytic activity

The catalytic activity measurements were carried out under atmospheric pressure using a microwave reactor (SAIREM) consisting of a reaction chamber and microwave transparent walls. The output power of the microwave generator could be changed continuously from 0 to 2000 W at a fixed frequency of 2.45 GHz [4]. After 300 mg of catalyst was loaded into the chamber, it was pumped down for about 1 h. The chamber is connected to a vacuum system with typical base pressure of ~10^{-2} Torr maintain by a rotary vacuum pump. Once the pressure was stable, H_2 gas (15 ml/min) was introduced into the chamber, and then the microwave power increased to 120 W and maintained for 30 min to remove the surface oxide layer from the catalyst. After the chamber was purged with argon gas for ~ 45 min, the reactant gases were introduced into the system. A feed with a constant CH_4/CO_2 molar ratio of 1:1 was used throughout the experiments. The initial activity tests of the catalysts were investigated in the range of 400-600 W using steps of 50 W, while the stability test was carried out at a constant microwave power of 600 W for 30 h time-on-stream (TOS) with a gas flow rate of 85 mL/min.

The product composition was analyzed using an on-line gas chromatograph equipped with a Porapak Q column and a thermal conductivity detector (TCD). During the course of investigation, a number of runs were repeated to check for reproducibility in the experimental results. Typical errors were in the range of ±2%. The conversions of CH_4 and CO_2 were calculated by means of the following equations:

$$CH_4 \text{ conversion, } \% = [(H_2)_{out}/2]/[(CH_4)_{out} + (H_2)_{out}/2] \times 100 \quad (1)$$

$$CO_2 \text{ conversion, } \% = [(CO)_{out}/2]/[(CO_2)_{out} + (CO)_{out}/2] \times 100 \quad (2)$$

Where $(CH_4)_{out}$, $(H_2)_{out}$, $(CO_2)_{out}$ and $(CO)_{out}$ are the concentrations of CH_4, H_2, CO_2 and CO as the effluent gas, respectively.

3. Results and discussion

3.1. Structure of perovskite precursors

Fig. 1 shows the XRD profiles of the perovskite precursors of the three samples. The formation of perovskite can be found. It is known that the size mismatch between A and B sites in perovskite structure can create a certain level of internal stress causing lattice distortion [31]. The distortion/internal stress in this study may also be created by partially replacing smaller Ni^{3+} with Cr^{3+} ions and was expected to transform the crystal structure of $LaCr_{1-x}Ni_xO_{3-\delta}$ (LCNs) from either orthorhombic phase to rhombohedral phase or a possible formation of the two phases, as to be discussed below in details.

3.1.1. Microstructure analysis

Figs. 1a-c show the structural identification of LCNs composites including LCN-1, LCN-4 and LCN-7 whose crystal structures were deduced using the standard Rietveld techniques (Table 1). *It can be seen that only typical diffraction peaks of perovskite phases were formed. However, the simulation pattern using* Le Bail and Rietveld refinement confirms the phase composition of the three samples that LCN-1 is composed of 76.52% orthorhombic phase, 20.15% NiO and 3.33% $NiCr_2O_4$, and LCN-4 is composed of 49.33% orthorhombic phase, 31.99% NiO and 18.67% rhombohedral phase, and LCN-7 is composed of 60.40% orthorhombic phase, 19.73% NiO and 11.87% rhombohedral phase. The structural parameters of each phase have been listed in Table 1. Table 1 also presents the refinements converge to reliability factors, with relatively low factor values indicating good fittings. The above results illustrate that the *phase segragation occurs in the three samples where besides the perovskite structures* (orthorhombic phase and rhombohedral phase in LCN4 and LCN-7 and orthorhombic phase in LCN-1), NiO can be identified in all the three samples and a low amount of $NiCr_2O_4$ can be found in LCN-1. The phase segregation should be attributed to the mismatch of La ions, Ni ions and Cr ions in perovskite structure. *Since no typical XRD peaks of NiO phase were formed, in principle these NiO particles identified by Le Bail and Rietveld refinement should be very small and be closely attached on the surface of perovskite structure.*

The size mismatch between the Ni^{3+} and Cr^{3+} in B sites was expected to affect the microstructure. Fig. 2a demonstrates a high yield of nanowires of 10-15 μm in length while a single flower-like LCN-1 crystal contains a core extended by a few branches arranged in a pillared structure. In Fig. 2b, the 3-phase composite LCN-4 exhibits egg-like morphology. But LCN-7 shows agglomerates consisting of interconnected nanoparticles (Fig. 2c). Fig. 2d shows the layered structure of LCN-1 with different width (4–24 nm). The egg-like morphology of LCN-4 is confirmed by HRTEM micrographs (Fig. 2e), while the interconnected nanoparticles of LCN-7 (20−100 nm) are clearly seen in Figure 2f. These distinct variations in the morphology of the samples should be caused by the evolution of *the substitution of Cr for Ni.* Totally, it can be seen that the ratio of Cr/Ni can impact the morphology of the catalyst samples clearly.

3.1.2. Structure for oxygen mobility

Structural defects always occur in perovskites due to deficiencies in the cations of A or B, which influences the oxygen mobility and the catalytic properties. We investigated the evolution of the oxygen of LCNs by employing temperature-programmed desorption (TPD) of O_2 monitored with a mass spectrometer. Fig. 3a presents the O_2-TPD spectra (*m/e* = 32) from LCN-1, LCN-4 and LCN-7, where various oxygen desorption processes can be observed. On LCN-1, the oxygen desorption process can be divided into three stages. The first one is very slow and flat from 460 to 600 °C and the second one is a small desorption peak with the temperature range of 600−650 °C and a maximum value at 625 °C and the third one is a big peak in the range from 650 to above 850 °C. On LCN-4, four oxygen desorption stages are identified. The first one is a low shoulder peak from 430 to 575 °C and the second one is a small peak from 575 to 660 °C with a maximum value at 618 °C and

the third one is a big peak from 660 to 800 °C with a maximum value at 765 °C and the fourth one is from 805 to above 850 °C. On LCN-7, the oxygen desorption can be divided into two stages. The first one is a very slow process from 465 to 745 °C and the second one is a small peak from 745 to 810 °C with a maximum value at 795 °C.

According to the literatrue [33-35], the first two stages in low temperature range of oxygen desorption on LCN-1 and LCN-4, which are small with broadened shape, are commonly assigned to two kinds of oxygen species with different bonding strength present on the surface of perovskite-type materials and the third large desorption stage at high temperature represents evolution of lattice oxygen. The former are attributed to the desorption of oxygen weakly chemisorbed on the surface [33,34] and the latter is related to the reduction of B cations (Ni) to lower oxidation state in ABO_3 structure [33,35]. The foruth desorption process above 800 °C on LCN-4 may be attributed to the oxygen in the deep bulk of perovskite lattice. The oxygen desorption process from 465-745 °C on LCN-7 is in the range of surface adsorbed oxygen of perovskite lattice and the oxygen desorption above 745 °C is attributed to the oxygen of the bulk perovskite lattice as described as above. It is accepted that charge compensation is required and the increase of the amount of released oxygen from the surface of the perovskite materials is caused when the substitution of A or B sites are partially substituted with an ion of different oxidation state [33-36]. In the case of the substitution of Cr for Ni, electroneutrality at the presence of Cr^{6+} (showed by XPS results of LCN-1 and LCN-4 in 3.1.4) can be achieved either by chemisorption of more oxygen or by shift of Ni^{3+} to lower oxidation state Ni^{2+}, which can cause the increase of the amount of the desorption oxygen in low temperature range [33,34,36]. The simualtion of the above XRD results has suggested the presence of NiO in the three perovsite precursors (Table 1 and Fig. 1). Therefore, the oxygen desorption signals of LCN-4 is more pronounced than those of LCN-7. For LCN-1, in which 90 % of Ni was substitued with Cr, the amount of the desorption oxygen is decreased due to too high doping amount of Cr. It should be specified that the contribution from the desorption of the oxygen from the segregated NiO identified by XRD on the three samples can be neglected by comparison with that from the perovskite materials [33,35,37].

Therefore, based on the oxygen desorption results of the materials, it can be seen that the perovskite matrix in LCN-4 possesses the highest oxygen mobility (low desorption temperature and high desorption amount) than that in LCN-1 and in LCN-7.

3.1.3. Structure for reducibility

The H_2-TPR represents the reducibility of the catalysts - an ability to liberate oxygen by reaction with H_2 [38]. Figs. 3b-d reveal the H_2-TPR profiles of LCN-1, LCN-4 and LCN-7. A mass spectrometer was employed to accurately determine the consumed H_2 only (*m/e* = 2) with no influence of other desorbed products such water (*m/e* = 18). On LCN-1 (Fig. 3b), there is a very small hydrogen consumption peak with a maximum at 250 °C and a big peak with a maximum at 495 °C. Fig. 3c reveals on LCN-4 the first of H_2 consumption peak with a maximum at 274 °C and the second peak with a maximum value at 446°C. On LCN-7 (Fig. 3d), the first hydrogen consumption process is very slow from 150 to 240 °C, and the second hydrogen consumption process is a big TPR peak with the maximum at 515 °C. On the three samples, the first hydrogen consumption process is assigned to the reduction of Ni^{3+} to Ni^{2+} and the second one belongs to that of Ni^{2+} to Ni^0 in perovskite and the segregated NiO phases because Cr^{3+} and La^{3+} are both difficult to be reduced under these conditions and the amount of Cr^{6+} can be neglected [18,39]. The biggest TPR peak for the reduction of Ni^{3+} to Ni^{2+} and the lowest reduction temperature of Ni^{2+} to Ni^0 of LCN-4 indicates the most available oxygen in the low temperature range for a rapid migration of the lattice oxygen from the bulk to the surface among three samples and hence LCN-4 shows the strongest migration mobility of lattice oxygen among three samples, then LCN-1 and LCN-7, which is consistent with O_2-TPD analysis (Fig. 3a).

3.1.4. Structure regarding chemical bonding states

The chemical bonding states of elements were examined by XPS. Fig. 4 shows the core level spectra for Cr 2p, O 1s and Fig. 5 shows those of Ni $2p_{3/2}$ in the reduced LCN-1, LCN-4 and LCN-7. In Fig. 4a, the Cr $2p_{3/2}$ spectra show peaks around 576.2 and 578.2 eV assigned to Cr^{3+} in O^{2-}–Cr^{3+}–O^{2-} and Cr^{6+} in O^{2-}–Cr^{6+}–O^{2-}, respectively [40]. It can be seen that in the reduced samples, there existed only Cr^{3+} in LCN-7 and majority of Cr are Cr^{3+} in LCN-1 and LCN-4 together with a small amount of Cr^{6+}. The O 1s spectra are also investigated after reduction (Fig. 4b), which can be deconvoluted into two peaks. In the three samples, two oxygen peaks were observed at 529.0 and 531.5 eV, assigned to O^{2-} in O^{2-}–Ni^{2+}–O^{2-} and O^{2-}–Ni^{3+}–O^{2-}, respectively (Fig. 4b) [41]. Figs. 5a-c shows the binging energy of Ni$2p_{3/2}$ in the three samples, which can be deconvoluted into three peaks at around 852.5, 854.0 and 857.5 eV, assigned to Ni^0, Ni^{2+} and Ni^{3+}, respectively [41]. Since majority of Cr is in the state of Cr^{3+}, the identification of Ni^{3+} in the three samples indicates the presence of perovskite LaNi(Cr)O_3 structure. The atomic ratio of Ni^{3+}:Ni^{2+}:Ni^0 is 32%:53%:15%, 48%:12%:40% and 33%:55%:12% in LCN-1, LCN-4 and LCN-7, respectively. Therefore, the order of the content of Ni^0 in the three samples is LCN-4 > LCN-1 > LCN-7 and that of the content of perovskite is LCN-4 > LCN-7 ≈ LCN-1. *By comparison with the NiO content obtained from the simulation of XRD profiles (Fig.1 and Table 1), it may be concluded that Ni^0 in LCN-1and LCN-7 is mainly reduced from the segregated NiO phase and Ni^0 in LCN-4 is derived from both the segregated NiO phase and perovskite phases. The results also strongly indicate that the interaction between the segregated NiO phase and the perovskite phase should be very strong and could hinder NiO to be reduced, which is consistent with the above XRD results.*

3.2. Impact of the structure on CO_2 reforming of methane

We investigated the catalytic activity of LCNs composite catalysts (structures shown in Table 1) in DRM under microwave irradiation (Fig. 6). *DRM is an endothermic reaction and requires high temperatures (>700°C) for achieving industrially relevant conversions (Eq. (3)).* Since the microwave absorption ability are different from each samples, the dependence of temperature on the catalyst surface on the microwave heating power were measured during the reaction using an infrared temperature sensor attached to the microwave reactor (Table 2).

$$CH_4 + CO_2 \rightarrow 2CO + 2H_2 \quad (3)$$

Figs. 6a and b reveal that the conversions follow the order LCN-4 > LCN-1 > LCN-7. Fig. 6a shows that LCN-4 exhibits ~73% higher methane conversion at 550 W than LCN-1, while the least performance is observed on LCN-7. Also, the coversion of pure $LaCrO_3$ was less than 4 % even at 600 W. All samples exhibit high CO/H_2 molar ratios (1.2−1.6) due to the reducing of the H_2 formation rate for water formation [42]. To compare their performance under the same temperature of the catalyst, CH_4 conversions of the LCN catalysts at 820 and 960 °C were compared and follow the same order: LCN-7 < LCN-1 < LCN-4 (Fig. 6c), similar to the conversion rates at different microwave power (Figs. 6a and b). It can be found that the order of the activity of LCNs is consistent with the oxygen mobility of the lattice (Figs. 3 and 4). Additionally, the content of Ni^0 indicates the possibly available amount of Ni^0 in the catalyst during DRM. From the above XPS results, it has been found that the order of the content of Ni^0 in the three reduced catalysts is LCN-4 >LCN-1 > LCN-7, which indicates that the most Ni^0 is available in LCN-4, then LCN-1 and LCN-7. It should be pointed out that according to the above results and discussion, all the Ni^0 have the strong interaction with the remaining perovskite structure whether they are reduced from the segregated NiO phase or perovskite phases. Therefore, the activity of LCNs may be dependent on the oxygen mobility and the content of Ni^0 in the catalysts.

Since it is vital for these catalysts to remain stable during the reforming reaction, their long-term stability was investigated. Fig. 6d presents the long-term stability of LCNs conducted for a time-on-stream (TOS) of 30 h. A gradual decline in CH_4 conversion is seen for all LCNs during the first 7 h, but LCN-4 and LCN-1 demonstrate respectively stable conversion rates of ~67% and ~46% after 8 h. From the XPS results, it has been known that LCN-4 has higher content of perovskite structure and higher

oxygen mobility than LCN-1, which indicates more oxygen possessing higher mobility in the oxide matrix of LCN-4, preventing the sintering of the highly-dispersed Ni particles at high reaction temperature of DRM. Therefore, LCN-4 shows the higher stability of the Ni particles than that of LCN-1, as illustrated as Fig. 6d. We thus conclude that the catalytic performance of LCNs in DRM is dependent on the oxygen mobility of composite oxide matrix, the content of the reduced Ni^0 and the content of the remaining perovskite structure.

3.3. Mechanisms

In this study, DRM under microwave irradiation is produced via a selective heating mechanism; since the absorption of microwave radiation solely depends on the properties of the target materials [3]. We systematically analyzed the possible mechanisms of DRM on $LaCr_{1-x}Ni_xO_{3-\delta}$ perovskite catalysts (LCN-1 and LCN-4) by investigating the *in situ* CH_4/CO_2 temperature programmed reaction (CH_4/CO_2 TPR).

During microwave-induced DRM, carbonaceous materials are formed via CH_4 cracking (Eq. (4)) and Boudouard reaction (Eq. (5)), together with other reactions such as CO_2 activation (Eq. (6)) and CO_2 gasification of carbon species (Eq. (7)) [42]. CO_2 provides O* and CO upon activation on the active sites (Eq. (6)), while CH_4 provides H* and CH_x^* (Eq. (8)). If a significant quantity of oxygen atom is available, the carbon could convert into CO (Eq. (9)) and the surface H* from the CH_4 favors the formation of H_2O (Eq. (10)) and CH_x^* favors oxidation into CO (Eq. (11)) [37].

$$CH_4 + 5^* \rightleftharpoons C^* + 2H_2^* \quad (4)$$

$$2CO^* \rightleftharpoons C^* + CO_2^* \quad (5)$$

$$CO_2 + 2^* \rightleftharpoons CO^* + O^* \quad (6)$$

$$CO_2^* + C^* \rightleftharpoons 2CO^* \quad (7)$$

$$CH_4 + (5-x)^* \rightleftharpoons CH_x^* + (4-x)H^* \quad (8)$$

$$C^* + O^* \rightleftharpoons CO^* \quad (9)$$

$$O^* + 2H^* \rightleftharpoons H_2O^* \quad (10)$$

$$O^* + CH_x^* \rightleftharpoons CO^* + xH^* \quad (11)$$

Figs. 7a and b reveals that the in situ CH_4/CO_2 TPR proceeds. It can be seen that the dependence of signal intensity of the related species (water, H_2, CH_4 and CO_2) upon temperature on LCN-1 are similar with that on LCN-4, indicating that the reaction mechanism on LCN-1 is the same as that on LCN-4. However, on LCN-1, CH_4 activation (Eq. (4) and (8)) CO_2 dissociation (Eq. (6) occur from 470 °C (Figure 7a), which is suggested by the formation of carbon species (C*), CO, H_2 and H_2O, while those take place on LCN-4 from 447 °C meaning that LCN-4 is more active than LCN-1, which is consistent with the above results in Figs. 6a–c. Additionally, it can be seen that below 700 °C a much faster rate of CO_2 dissociation on both LCN-1 and LCN-4 than that of CH_4 pyrolysis, suggesting a higher formation rate of CO* and O* (Eq. (6) and (7)). The faster dissociation of CO_2 indicates i) a higher conversion of CO_2 (Fig. 6a and b); ii) a high oxygen mobility on the surface of LCN-1 and LCN-4 (Eq. (6)); iii) a ratio of CO/H_2 higher than 1.0; iv) the formation of H_2O (Eq. (10)); v) a low formation rate of coke (Eq. (5), (7) and (9)). At temperatures higher than 700 °C, both CH_4 activation and CO_2 dissociation proceed at almost the same rate, leading to a faster increase in H_2 formation than that in H_2O formation. Therefore, it can be deduced from this result that the oxygen mobility takes an important role in enhancing the conversion of the reactants and the reaction stability by prohibiting the formation of coke on this type of catalysts.

4. Conclusion

The structure of Ni catalysts derived from Cr-doped $LaNiO_3$ (LCNs) perovskite-like structure were influenced by the ratio of Ni^{3+} and Cr^{3+}. The mismatch of La^{3+}, Ni^{3+} and Cr^{3+} causes the phase segregation of the composite oxides. The catalytic performance of the Ni catalysts in DRM under microwave irradiation is dependent on the oxygen mobility of composite oxide matrix, the content of the reduced Ni^0 and the content of the perovskite structure. The oxygen mobility in the oxygen matrix of LCNs can enhance the conversion of CO_2. LCN-4, which has a Cr/Ni atomic ratio of 0.6/0.4 and possesses the highest content of both Ni metal and perovskite matrix among LCNs, exhibited the highest methane and CO_2 conversion rate and demonstrated a long-term stability of ~67% on methane conversion for a time-on-stream of 30 h.

Acknowledgments

The first author acknowledges the support from International Postgraduate Research Scholarship (IPRS) and UQ Centennial Scholarship (UQ Cent). Zhonghua Zhu also likes to thank the financial support by the Australian Research Council (FT120100720).

References

[1] T. Odedairo, J. Chen and Z. Zhu, *J. Phys. Chem. C* 2013, 117, 21288−21302.

[2] T. Odedairo, J. Chen and Z. Zhu, *Catal. Commun*. 2013, 31, 25−31.

[3] T. Odedairo, J. Ma, Y. Gu, J. Chen, X. S. Zhao, Z. Zhu, *J. Mater. Chem. A* 2014, 2, 1418−1428.

[4] T. Odedairo, J. Ma, J. Chen, S. B. Wang and Z. Zhu, *J. Solid State Chem.* 2016, 233, 166−177.

[5] Y. Zhang, S. Zhang, H. H. Lou, J. L. Gossage, T. J. Benson, *Chem. Eng. Technol.* 2014, 37, 1493−1499.

[6] M. Khajenoori, M. Rezaei, F. Meshkani, *Chem. Eng. Technol.* 2014, 37, 957−963.

[7] H. Zhang, M. Li, P. Xiao, D. Liu, C.-J. Zou, *Chem. Eng. Technol*. 2013, 36, 1701–1707.

[8] S. O. Aydinoglu, A. E. Aksoylu, *Int. J. Hydrogen Energy* 2011, 36, 2950−2959.

[9] J. Guo, H. Lou, H. Zhao, D. Chai, X. Zheng, *Appl. Catal. A* 2004, 273, 75−82.

[10] *D. Liu, X. Y. Quek, H. H. Adeline Wah, G. Zeng, Y. Li, Y. Yang, Catal. Today 2009, 148, 243−250.*

[11] *G. Zeng, J. Shao, R. Gu, Y. Li, Catal. Today 2014, 233, 31−37.*

[12] *G. Zeng, Q. Liu, R. Gu, L. Zhang, Y. Li, Catal. Today 2011, 178, 206−213.*

[13] *R. Gu, G. Zeng, J. Shao, Y. Liu, J. W. Schwank, Y. Li, Frontiers Chem. Sci. Eng. 2013, 7, 270−278.*

[14] S. Zhang, S. Muratsugu, N. Ishiguro, M. Tada, *ACS Catal*. 2013, 3, 1855−1864.

[15] Z. Li, L. Mo, Y. Kathiraser, S. Kawi, *ACS Catal*. 2014, 4, 1526−1536.

[16] M. Yu, Y. A. Zhu, Y. Lu, G. Tong, K. Zhu, X. Zhou, *Appl. Catal. B* 2015, 165, 43−56.

[17] H. Ay, D. Uner, *Appl. Catal. B* 2015, 179, 128−138.

[18] T. Wu, Q. Zhang, W. Cai, P. Zhang, X. Song, Z. Sun, L. Gao, *Appl. Catal. A* 2015, 503, 94−102.

[19] T. Odedairo, W. Zhou, J. Chen, Z. Zhu, *RSC Adv.* 2014, 4, 21306-21312.

[20] S. K. Chawla, M. George, F. Patel, S. Patel, *Procedia Eng*. 2013, 51, 461-466

[21] G. Moradi, H. Hemmati, M. Rahmanzadeh, *Chem. Eng. Technol*. 2013, 36, 575−580.

[22] S. Pavlova, L. Kapokova, R. Bunina, G. Alikina, N. Sazonova, T. Krieger, A. Ishchenko, V. Rogov, R. Gulyaev, V. Sadykova, C. Mirodatos, *Catal. Sci. Technol*. 2012, 2, 2099–2108.

[23] T. Odedairo, J. Ma, Y. Gu, W. Zhou, J. Jin, X.S. Zhao, Z. Zhu, *Nanotechnology* 2014, 25, 495604−495614.

[24] J. A. Menendez, A. Arenillas, B. Fidalgo, Y. Fernandez, L. Zubizarreta, E. G. Calvo, J. M. Bermudez, *Fuel Process Technol*. 2010, 91, 1−8.

[25] D. Sab-Jose-Alonso, J. Juan-Juan, M. J. Illan-Gomez, M. C. Roman-Martinez, *Appl. Catal. A* 2009, 371, 54−59.

[26] B. Fidalgo, Y. Fernandez, L. Zubizarreta, A. Arenillas, A. Dominguez, J.J. Pis, J.A. Menendez, *Appl. Surf. Sci*. 2008, 254, 3553-3557.

[27] B. Fidalgo, A. Dominguez, J. J. Pis, J. A. Menendez, *Int. J. Hydrogen Energy* 2008, 33, 4337–4344.

[28] M. Panneerselvam, K. J. Rao, *J. Mater. Chem*., 2003, 13, 596–601.

[29] Y. N. Chen, Z. J. Wang, *J. Am. Ceram. Soc*. 2013, 96, 90–95.

[30] B. C. H. Steele, P. H. Middleton, R. A. Rudkin, *Solid State Ionics*, 1990, 40, 388−393.

[31] J. Yang, *Acta Cryst.*, 2008, 64, 281−286.

[32] M. Iwasaki, H. Takizawa, K. Uheda, T. Endoa, M. Shimada*, J. Mater. Chem*., 1998, 8, 2765–2768.

[33] *B. Bialobok, J. Trawczynski, W. Mista, M. Zawadzki, Appl. Catal. B, 2007, 72, 395–403.*

[34] *S. Royer, D. Duprez, S. Kaliguine, Catal. Today 2006, 112, 99-102.*

[35] *L. Lisi, G. Bagnasco, P. Ciambelli, S. De Rossi, P. Porta, G. Russo, M. Turco, J. Solid State Chem. 1999, 146, 176-183.*

[36] *X. Peng, H. Lin, W. Shangguan, Z. Huang, Ind. Eng. Chem. Res. 2006, 45, 8822–8828.*

[37] *Y. Takasu, H. Niwa, Y. Matsuda, J. Catal., 1978, 51, 286–290.*

[38] Z. Wang, H. Wang, Y. Liu, *RSC Adv.,* 2013, 3, 10027−10036.

[39] V. B. Vert, F. V. Melo, L. Navarrete, José M. Serra, *Appl. Catal. B* 2012, 115\116, 346– 356.

[40] M. Aronniemi, J. Sainio, J. Lahtinen, *Surf. Sci.,* 2005, 578, 108−123.

[41] C. D. Wanger, W. M. Riggs, L. E. Davis, J. F. Moulder, G. E. Muilenberg, Handbook of X-ray Photoelectron Spectroscopy Perkin-Elmer Corp., Physical Electronics Division, Eden Prairie, Minnesota, USA 1979.

[42] A. Yamaguchi, E. Iglesia, *J. Catal.,* 2010, 274, 52−63.

Tables

Table 1 Refined structural parameters of $LaCr_{1-x}Ni_xO_{3-\delta}$ (x = 0.1, 0.4 and 0.7).

Parameter	LCN-1 (x = 0.1)	LCN-4 (x = 0.4)	LCN-7 (x = 0.7)
Lattice Constants			
1st phase (Major)	$LaCr_{1-x}Ni_xO_{3-\delta}$	$LaCr_{1-x}Ni_xO_{3-\delta}$	$LaCr_{1-x}Ni_xO_{3-\delta}$
Fraction (%)	76.52	49.33	60.40
a (Å)	5.5185 (4)	5.4766 (9)	5.4664 (3)
b (Å)	5.4817 (3)	5.5137 (9)	5.4664 (3)
c (Å)	7.7665 (1)	7.7747 (4)	13.2165 (1)
crystal structure	orthorhombic	orthorhombic	rhombohedral
Space group	*Pbnm*	*Pbnm*	*R3c*
Cr/Ni−O1× 2 (Å)	1.9783	1.9325	
Cr/Ni−O2× 2 (Å)	1.9243	1.5003	
Cr/Ni−O2× 2 (Å)	2.0209	2.3573	
(Cr/Ni−O) (Å)	1.9745	1.9300	1.9256
Cr−O1−Cr × 2 (°)	157.9397	173.0869	
Ni−O1−Ni × 2 (°)	157.9397	173.0869	
Cr−O2−Cr × 4 (°)	160.7147	170.2813	
Ni−O2−Ni × 4 (°)	160.7147	170.2813	
Cr−O−Cr (°)			176.6692
Ni−O−Ni (°)			176.6692
2nd phase	NiO	NiO	NiO
Fraction (%)	20.15	31.99	19.73
a (Å)	4.1815 (2)	4.1816 (2)	4.1821 (9)
crystal structure	cubic	cubic	cubic
Space group	*Fm-3m*	*Fm-3m*	*Fm-3m*
3rd phase	Traces ($NiCr_2O_4$)	$LaCr_{1-x}Ni_xO_{3-\delta}$	$LaCr_{1-x}Ni_xO_{3-\delta}$
Fraction (%)	3.33	18.67	11.87
a (Å)	8.3354 (4)	5.4688 (7)	5.4616 (5)
b (Å)	-	5.4688 (7)	5.5130 (3)

c (Å)	-	13.2340 (0)	7.7451 (3)
crystal structure	cubic	rhombohedral	orthorhombic
Space group	*Fd-3m*	*R3c*	*Pbnm*
		R-Factors	
χ^2	1.32	1.73	2.23
R_p	3.51	4.25	5.47
R_{wp}	4.47	5.98	7.48

Table 2 Temperature on the surface of catalysts during the catalytic reaction

	LCN-1	LCN-4	LCN-7
Microwave power	Temperature (°C)		
400 W	771	762	804
450 W	811	806	825
500 W	828	821	918
550 W	874	852	960
600 W	967	961	1105

Figures

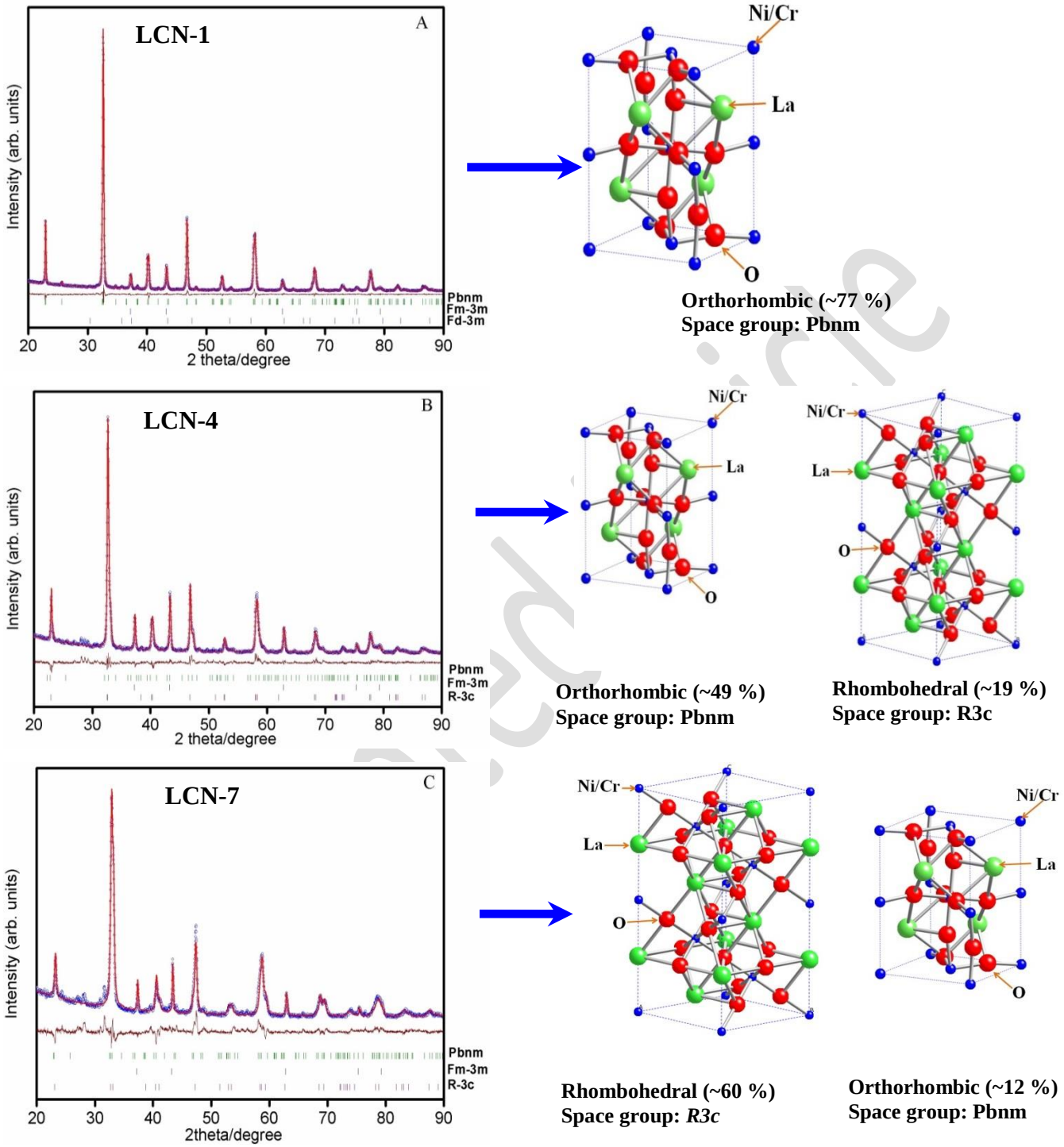

Fig. 1 Structural analysis of LCN-1, LCN-4 and LCN-7. Le Bail refined XRD pattern of $LaCr_{1-x}Ni_xO_{3-\delta}$ with experimental data (red dots), calculated profiles (blue line), difference curve (green line), and the calculated Bragg positions (vertical bar) for each phase.

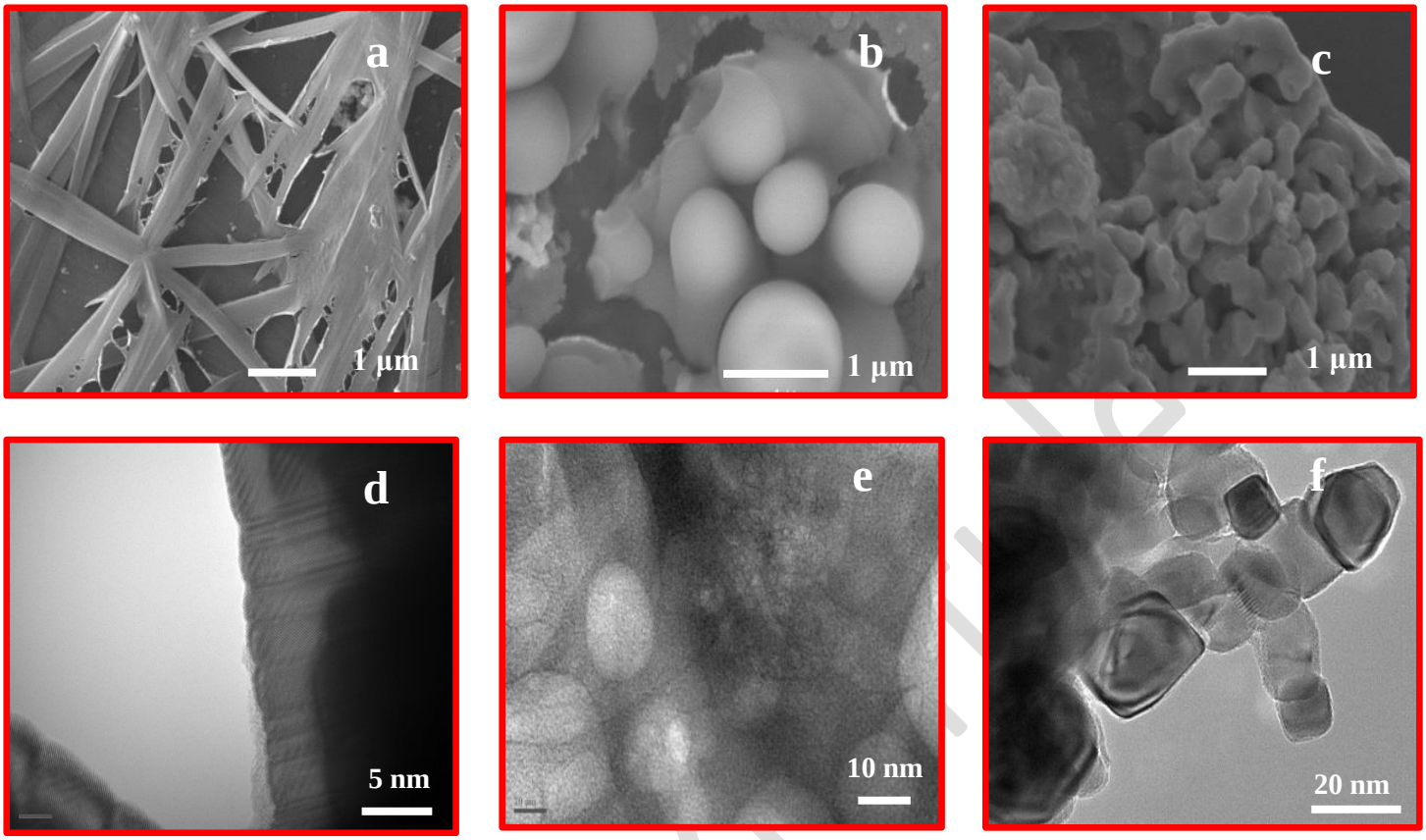

Fig. 2 FESEM (a–c) and HRTEM (d–f) micrographs of LCN-1, LCN-4 and LCN-7.

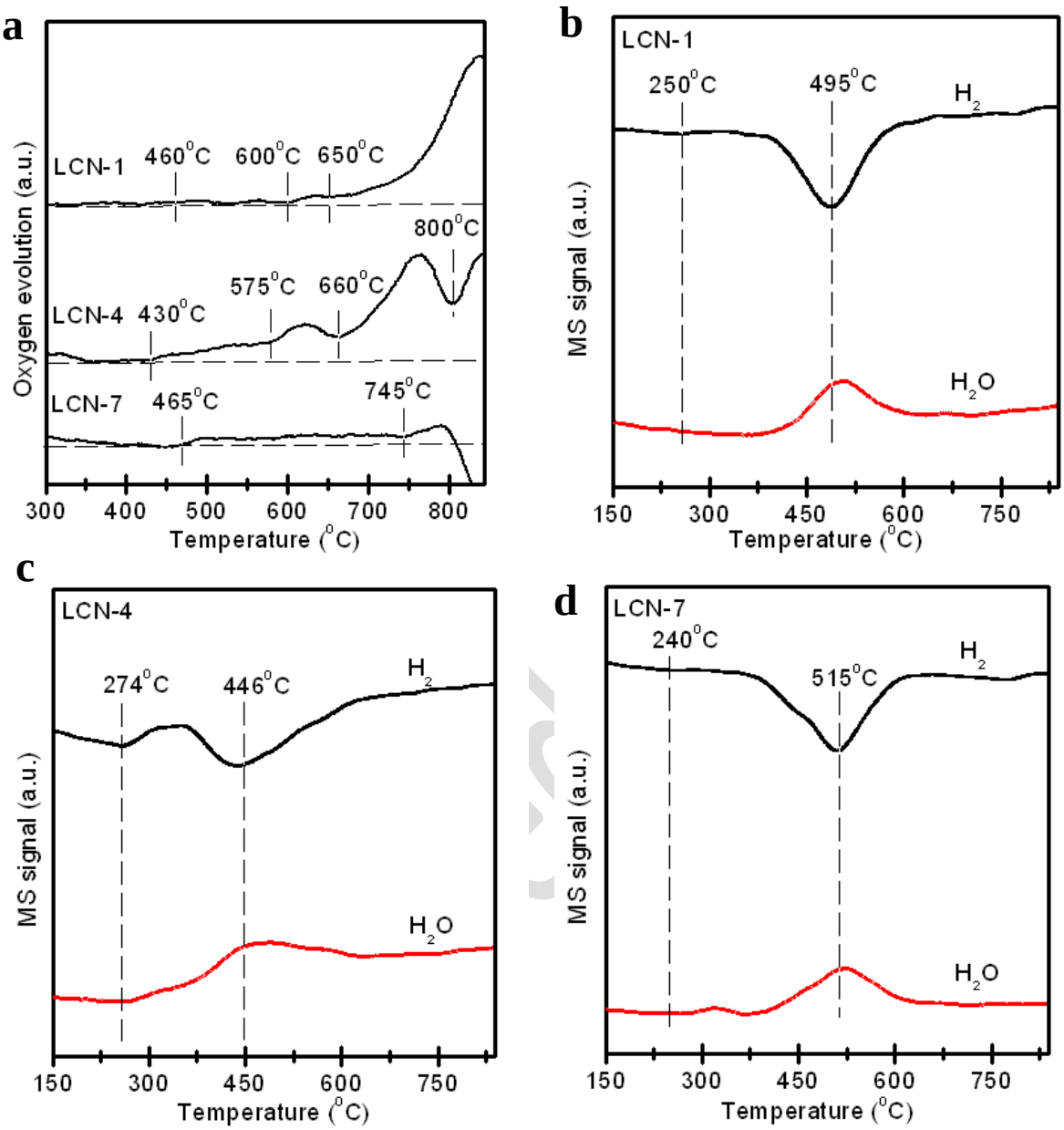

Fig. 3 Oxygen temperature-programmed desorption (O_2-TPD) (a) and hydrogen temperature-programmed reduction (H_2-TPR) profiles for LCN-1, LCN-4 and LCN-7 (b-d).

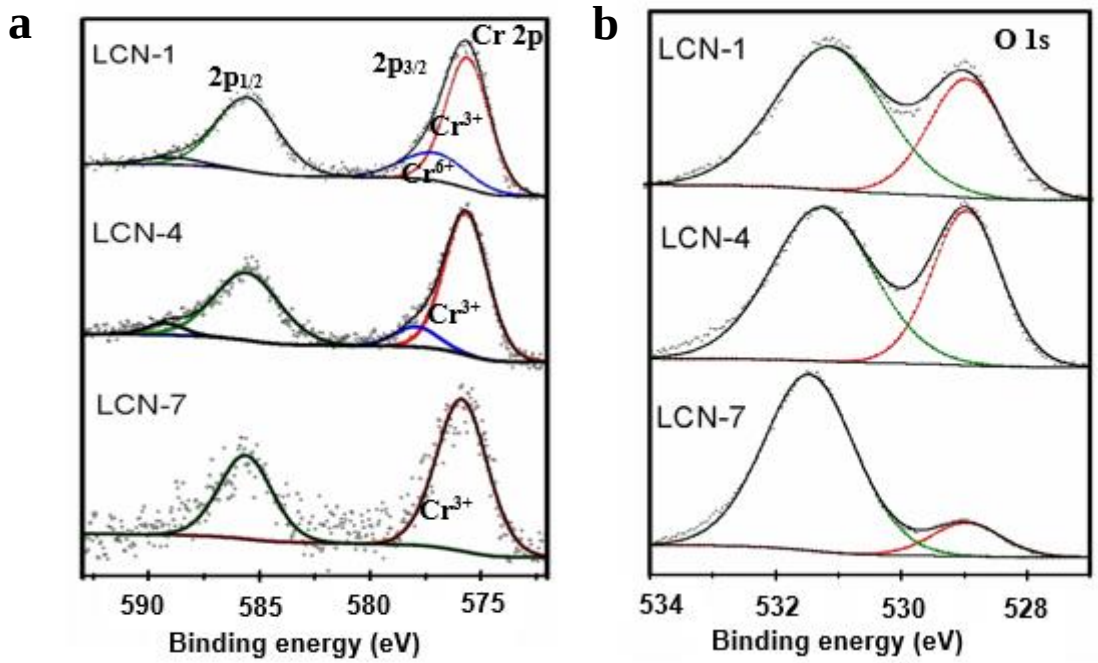

Fig. 4 XPS spectra of LCN catalysts: Cr 2p (a) and O 1s (b).

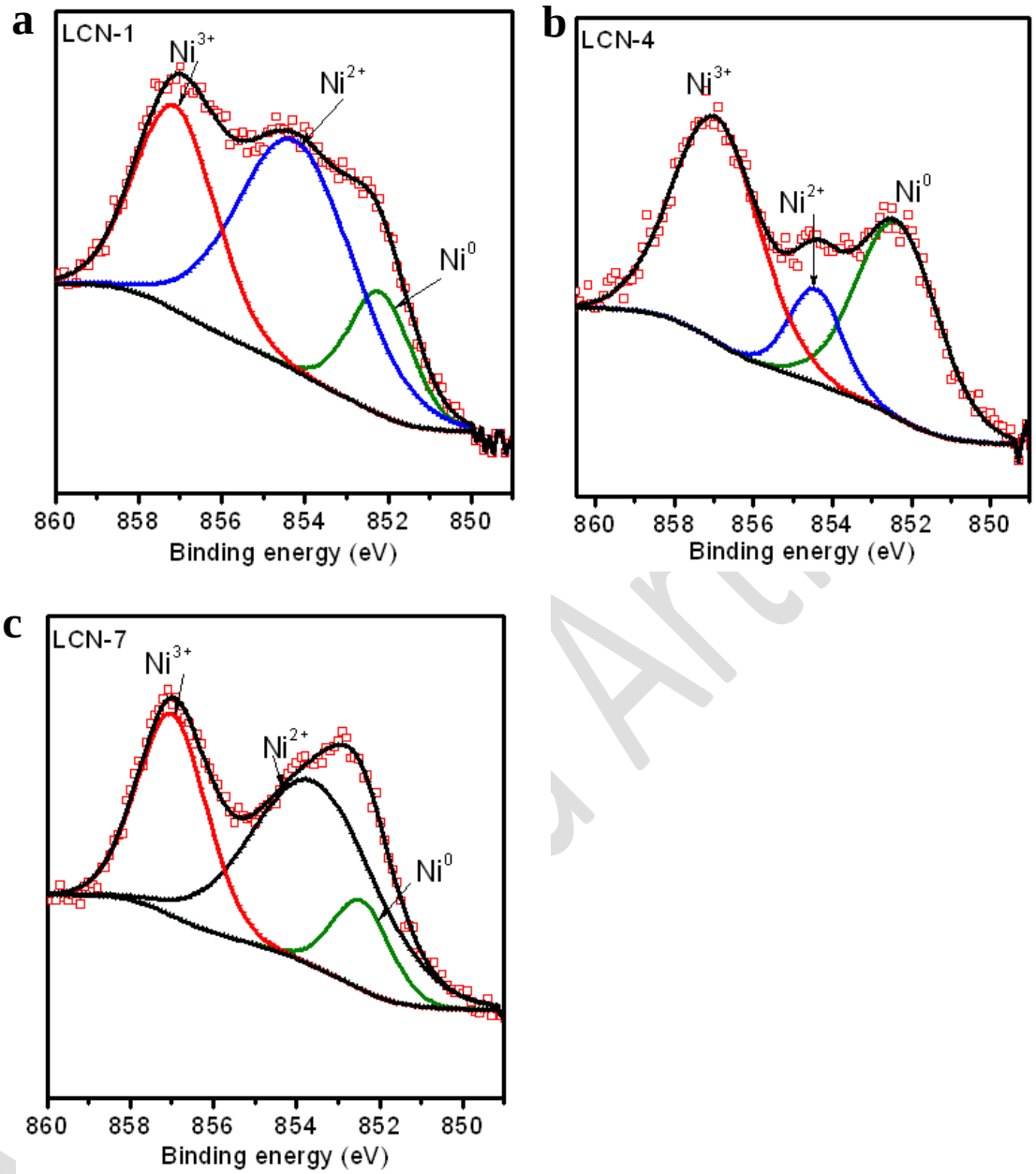

Fig. 5 XPS spectra of Ni of LCN catalysts: LCN-1(a), LCN-4 (b) and LCN-7.

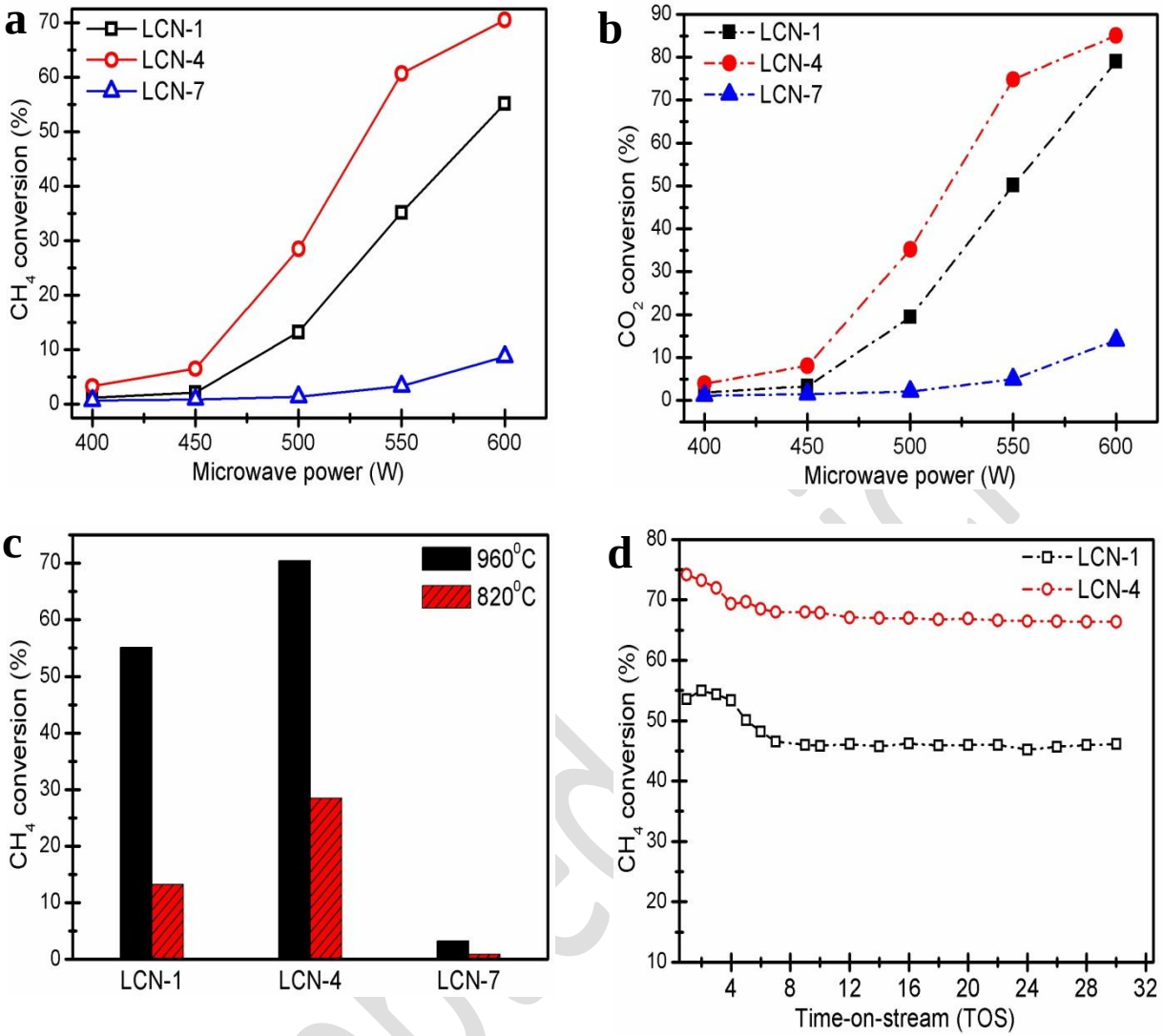

Fig. 6 Catalytic performance of LCNs in CO_2 reforming of methane: (a) Methane and (b) CO_2 conversion of LCN-1, LCN-4 and LCN-7 as a function of microwave power and (c) CH_4 conversion of LCN-1, LCN-4 and LCN-7 at similar reaction temperatures, and (d) stability test on LCN-1 and LCN-4 for 30 h time-on-stream (TOS).

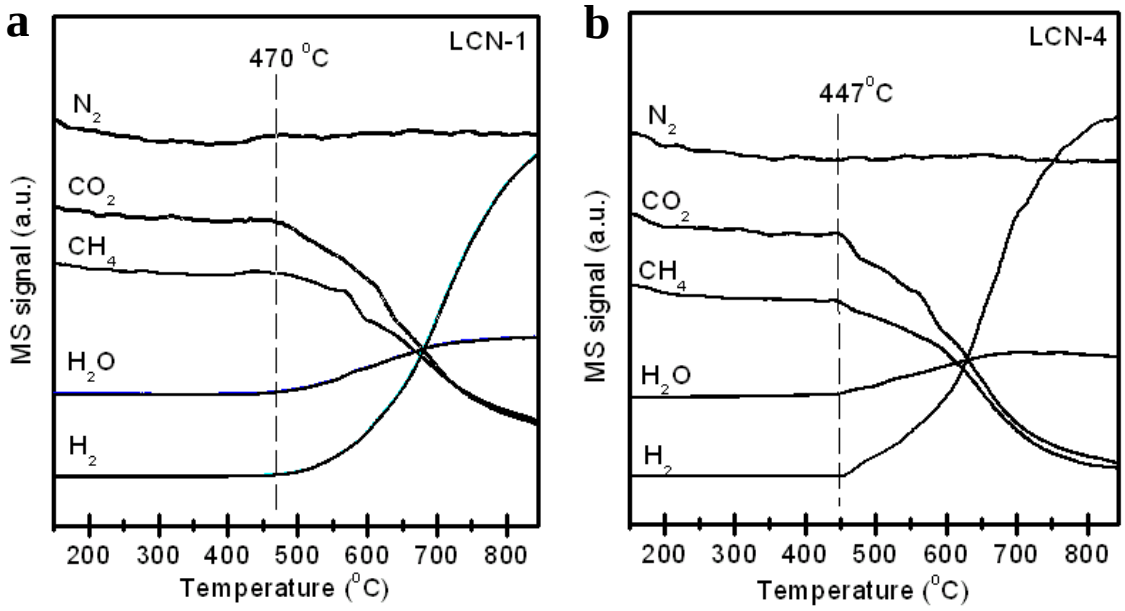

Fig. 7 *In situ* CO_2 reforming of methane on (a) LCN-1 and (b) LCN-4 with a gas flow of 10%CH_4/10%CO_2 in N_2 detected by mass spectrometer. A *m/e* ratio of 28 is the main peak for CO which overlaps with the peak for N_2.